Discontinuous boundary elements for steady-state fluid flow problems in discrete fracture networks

Composites Part B 309 (2026) 113084

Contents lists available at ScienceDirect

Composites Part B

journal homepage: www.elsevier.com/locate/composites

A modal-based shape optimization methodology for conventionally shaped patches in composite plate repair☆

Leonel Echer [a,b,*], Ozden O. Ochoa [c], Carlos Eduardo de Souza [b], Rogério J. Marczak [b]

[a] Department of Structural, Geotechnical and Building Engineering, Polytechnic University of Turin, Turin, TO 10129, Italy
[b] Department of Mechanical Engineering, Federal University of Rio Grande do Sul, Porto Alegre, RS 90050-170, Brazil
[c] Department of Mechanical Engineering, Texas A&M University, College Station, TX 77843-3123, United States of America

ARTICLE INFO

Keywords:
Laminate plates
Structural optimization
Repair patches
Patch shape
Modal response
Rupture load

ABSTRACT

Composite materials are known to excel in high-performance applications, particularly in the aerospace industry. Due to this fact, there is a growing concern regarding the maintenance, repair, and overhaul operations of such materials. Within this context, the best approaches for restoring the degraded mechanical properties of composites converge towards the use of fiber-reinforced adhesive patches. The present work proposes a novel methodology for the shape optimization of patches for the recovery of locally damaged composite plates. A shape optimization problem was formulated with the aim of minimizing the error associated with the modal response of the repaired structure to that of the undamaged one. Sequential linear programming was employed alongside an interior point algorithm to attain the optimized dimensions of rectangular single-sided patches, which were used in the restoration of simply supported damaged square panels. The damage was introduced by the mechanical removal of material along the central region. Modal and three-point bending tests were conducted to evaluate the performance of the patch repair. The modal response of the repaired panels indicated an efficiency of 98.2 % restoration of the first natural frequency. The effectiveness in terms of mechanical strength was 94.0 % in restoring the maximum resisted load, and 96.5 % in terms of the ultimate displacement.

1. Introduction

Approximately a decade ago, the emergence of contemporary aircraft models such as the Boeing 787, Airbus A350, and Bombardier CS300 (currently referred to as A220) symbolized the civil aviation industry's inclination towards substituting metallic alloys with advanced composites. In an effort to maximize the high specific strength, or strength-to-weight ratio, that is intrinsic to advanced materials, aircraft manufacturers significantly increased the use of composites in both secondary and primary components [1]. This trend has gained prominence in recent decades [2,3], which has led to an escalating concern regarding aviation safety [4,5]. Furthermore, as identified by the US Government Accountability Office (GAO), the progression of technology pertinent to structural repair and maintenance operations is essential to support the burgeoning demand for advanced composites at a sustainable growth level [6].

Furthermore, the wind energy sector is facing a significant demand for advanced tools that can enhance the operational longevity of wind turbines. Wind turbines present substantial environmental and economic challenges upon reaching their End of Life (EoL). The annual volume of waste generated from carbon fiber (CF) products is expected to reach 60.0 kt by 2026 and is forecasted to experience a significant increase in its growth trajectory by 2027, reaching 128.0 kt annually by the end of the decade. The majority of this waste is due to the EoL of first-generation wind turbines [7]. This situation is corroborated by the growing demand for CF in global markets, anticipated to reach 147 kt by the end of 2025, as depicted in Fig. 1, created using data sourced from [8,9].

The aerospace and energy industries use large and highly integrated composite structures, which are most prone to damage. Thus, risk events ending in localized damage, e.g., dents, cracks, and delamination, commonly result in the complete component's replacement, which

☆ This document is the result of the Ph.D. research project funded by the Coordination for the Improvement of Higher Education Personnel (CAPES), Brazil. Moreover, the present work was conducted at the Federal University of Rio Grande do Sul (UFRGS), and, as part of a short-term collaborative research, at the Texas A&M University (TAMU).

* Corresponding author at: Department of Structural, Geotechnical and Building Engineering, Polytechnic University of Turin, Turin, TO 10129, Italy.
E-mail addresses: leonel.echer@polito.it (L. Echer), oochoa@tamu.edu (O.O. Ochoa), ce.souza@ufrgs.br (C.E. de Souza), rato@mecanica.ufrgs.br (R.J. Marczak).

https://doi.org/10.1016/j.compositesb.2025.113084
Received 18 August 2025; Received in revised form 24 September 2025; Accepted 6 October 2025
Available online 10 October 2025

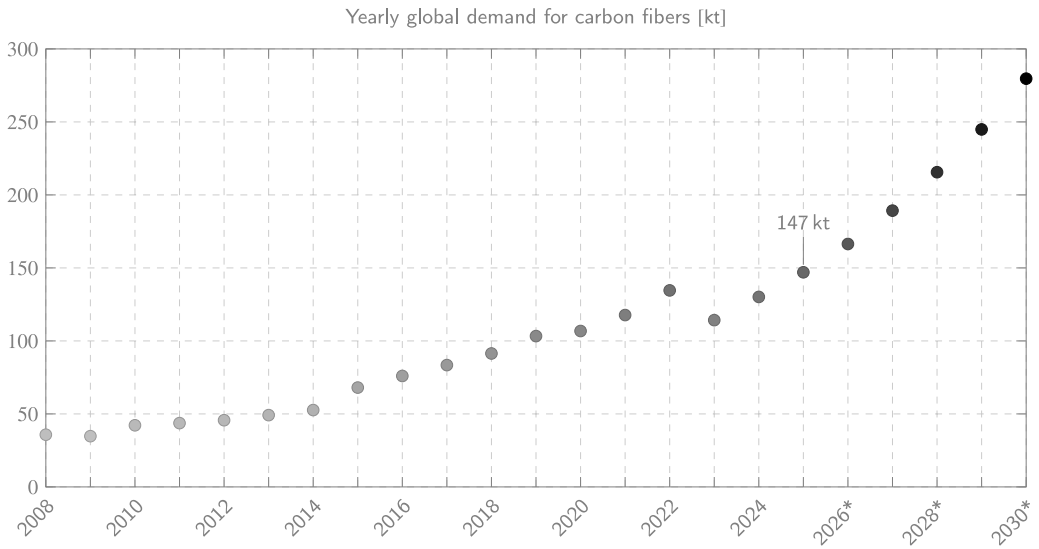

Fig. 1. Global trend for carbon fibers industry demand.

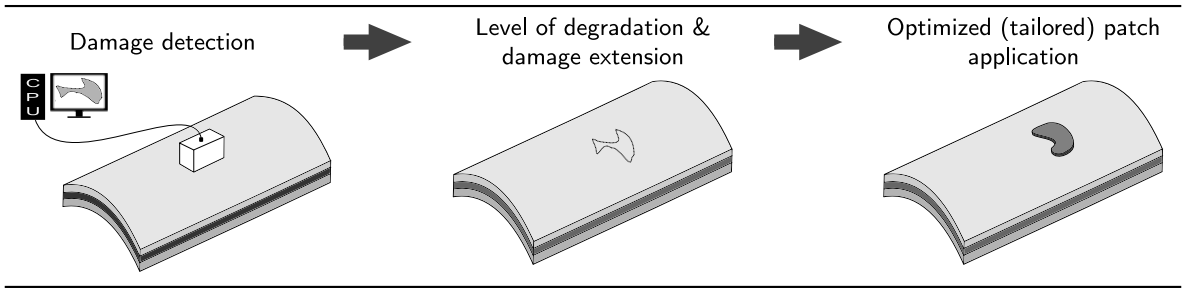

Fig. 2. Logical sequence for identifying and repairing a locally damaged composite with adhesive bonded repair patch.

is impractical and economically unwise. This situation underscores the need for sustainable options to extend the life of expensive composite damaged parts, which are, in practice, way more demanding than the usual aluminum/steel/titanium components' repair. In the current scenario, fiber-reinforced adhesive patches are the most promising and efficient way to restore or even improve the mechanical response of damaged composites [10]. The basic idea behind such a concept is illustrated in Fig. 2.

1.1. Fiber-reinforced repair patches

Since the early '70s, pioneering research conducted in the Australian Research Laboratories (ARL) [11] showed the efficiency of Fiber-Reinforced Repair Patches (FRRP) in the restoration of cracked metallic components. These early works, essentially empirical and restricted to military applications, were extraordinarily successful in reducing, more than 30 times, the Stress Intensity Factor (SIF) and preventing crack growth in locally damaged metallic sheets [12–14].

Due to their high efficiency and versatility, adhesively bonded FRRP had their application extended to civil aircraft in the early '90s [15]. However, civil aviation norms and regulations [16,17] are still very vague or restrictive regarding such tools. A key aspect of this restrictiveness lies in the distinction between primary and secondary structures. Currently, regulatory bodies like the Federal Aviation Administration (FAA) generally permit the use of solely adhesively bonded repairs on secondary aerostructures, which are not considered flight-critical. For primary structures, such as wings and fuselage frames, supplemental fastening methods are typically required to ensure fail-safe performance. The lack of a universal protocol to rule the use of repair patches results in different procedures adopted by each aircraft manufacturer [18,19]. Furthermore, even after decades of usage, there is still no consensus on the patches' geometrical configurations that are most efficient [10]. There is consensus, however, regarding the benefits of smaller repair patches [20,21]. Drawbacks such as humidity absorption, residual thermal stress due to curing, and aerodynamic modification are more likely to occur in patches covering larger surface areas. Thus, several authors have proposed, over the past decades, different shapes for fiber-reinforced repair patches with minimal surface area and, consequently, better efficiency. However, the vast majority of the approaches presented in the literature result in patches with unconventional shapes, as illustrated by Fig. 3.

The aforementioned unconventional patch shapes significantly increase the patch's efficiency. However, this is achieved at the cost of drastically escalating the repair procedure complexity. Some of the shapes presented by Fig. 3 are completely impractical for a field application. Most of these shapes could only be obtained through a variable-axial fiber layout, something possible [26–29] but still unattainable for practical applications [30–32].

A less invasive patching approach could be obtained by tailoring the patch's area of action to the damage extension, see Fig. 3. Furthermore, a patch covering an excessive surface, or oriented in a suboptimal direction, will probably result in material waste, over-stiffened regions, and aerodynamics/inertia alteration. A repair patch incorrectly designed might be more dangerous than no patch at all [10,33,34].

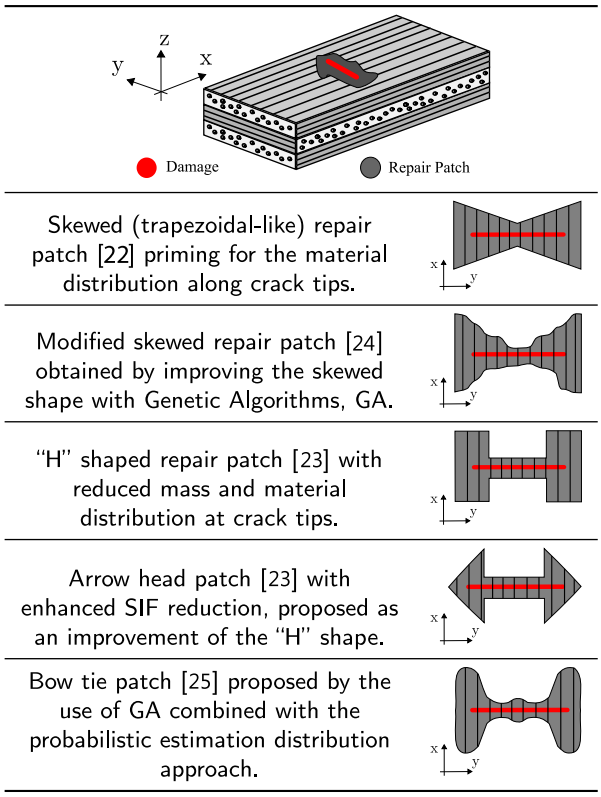

Fig. 3. Different unconventional repair shapes. See [22–25].

Aiming to circumvent these drawbacks, the present work proposes a methodology to systematically optimize the dimensions of fiber-reinforced repair patches with conventional geometrical shapes. While the proposed framework is adaptable, this study focuses on its application to damages prepared via local material removal, exemplified here by a partial-thickness oblong removal in an IM7/BMI flat quasi-isotropic panel, with the goal of restoring the plate's original modal response.

While the field of composite repair is mature and current methods effectively restore static properties, the design philosophy for patches often relies on stress reduction criteria (e.g., SIF) or simple stiffness matching. These approaches, however, frequently overlook two critical aspects for aerospace applications:

> **Structural Inertia**: Most optimization strategies neglect the mass addition of the patch, focusing solely on stiffness. This can alter the dynamic response of the component, which is critical for avoiding aeroelastic instabilities like flutter.
> **Practicality of Optimized Geometries**: Many academic studies utilizing advanced FEA, such as topology optimization, result in complex, unconventional patch shapes (e.g., bow-tie, H-shaped). While theoretically efficient, these geometries are often impractical for field-level MRO due to manufacturing and certification difficulties.

The novelty of this work lies in addressing these gaps. We propose a methodology that uses the modal response (i.e., natural frequency) as the primary optimization objective. This approach inherently accounts for both stiffness restoration and mass addition (structural inertia), offering a more holistic design criterion. Furthermore, the methodology presented herein is specifically tailored to optimize conventional, field-applicable geometries (rectangular and elliptical), bridging the gap between theoretical optimization and practical application.

1.2. Work overview

The present work aims to achieve repair patches with minimal area, covering just enough substrate surface to restore the damaged component to its original mechanical response.

The method introduced addresses the need to balance the component's stiffness before damage and after repair. To achieve this goal, the geometrical parameters of rectangular patches were optimized using mathematical programming (Section 2.2). This process involved a shape optimization problem aimed at matching the modal response of the repaired component to its original state, i.e., undamaged configuration. Modal tests were conducted with square flat panels before the damage, after damage (comparison solution), and after repair using the optimally designed patches, as detailed in Section 2.3.

Once an optimization-driven patch was defined, it was tested in the repair of composite panels containing a central region of localized damage. Once repaired, the panels were submitted to a three-point bending test until rupture. This allowed the patch's efficiency to be assessed in terms of its ability to restore both the modal response and mechanical strength.

2. Materials and methods

In the present study, specimens consisted of CFRP panels with localized damage, represented by a groove extending across the central region of the substrate (see Fig. 4(b)). This damaged configuration, achieved through mechanical material removal, reflects a typical procedure to prepare a surface with crack-like damage to receive a repair patch. Adhesively bonded repair patches were adopted to restore the mechanical response of such components. To simulate a real-life scenario where access to both sides of the damaged component is not feasible, the patches were defined as unbalanced, i.e., only covering the substrate's top surface. Moreover, the patches employed a rectangular geometry, and a single layer of fabric was used per patch. The patches' geometrical parameters were optimized through the shape optimization process to achieve the optimized configuration.

2.1. CFRP panels and patches

Fig. 4 illustrates the composite materials employed in this work. The substrate panels were flat, square IM7/BMI (5250-4) plates, as shown in Fig. 4(a). A total of ten specimens, with dimensions 304.8 mm × 304.8 mm × 3.9 mm, were analyzed. These IM7/BMI panels were fabricated using a 4-harness satin weave bi-axial (0/90) fabric. The material used for the repair patches, illustrated in Fig. 4(c), was a 5-harness satin weave, namely AS4 carbon fabric, which was used in combination with a commercially available epoxy resin (3501-6).

The mechanical properties for the IM7/BMI panels and AS4 patches are presented in Tables 1 and 2, respectively. These data were compiled from manufacturers' datasheets [35–38] and from the literature [39]. The mechanical properties presented in the aforementioned tables consider the materials as a unidirectional single-layer lamina.

The IM7/BMI substrate panels were labeled sequentially from PNL-00 to PNL-09. The first three plates (PNL-00, PNL-01, and PNL-02) were kept undamaged and employed as a comparison solution for all the tests conducted. The other seven panels were locally damaged by mechanical material removal. The damage geometry followed a stadium (oblong) shape as seen in the white marked central region of Fig. 4(b). The damage size was 139.70 mm × 9.53 mm, extending along the plates' center line horizontally. The damage region had rounded ends with a radius equal to 4.77 mm, a value slightly larger than the radius of the abrasive drill bits used to remove the material, i.e., 4.76 mm. The damage region extended through 75 % of the substrate's total thickness, which resulted in material removal through a depth of 2.9 mm. The only exception to that was specimen PNL-09, which was subjected to through-thickness damage, i.e., material removal that fully penetrated the parent plate. Thus, PNL-09 was used as a test case to evaluate the performance of the repair patch under damage conditions beyond those considered by the optimization algorithm.

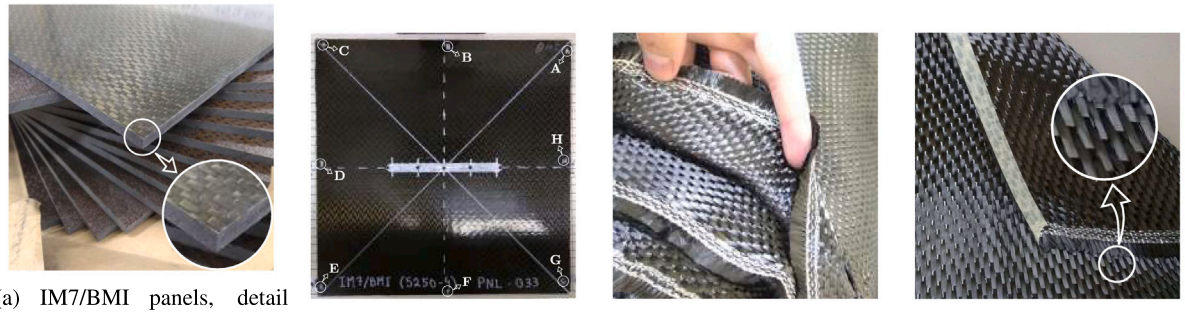

(a) IM7/BMI panels, detail view. (b) IM7/BMI panel top-surface. (c) AS4 - fabric. (d) AS4 - detail view.

Fig. 4. IM7/BMI square panels, substrate, and AS4 fabric used as repair patches.

Table 1
Mechanical properties for unidirectional lamina (0°): IM7/BMI (5250-4).

Elasticity modulus	E_{11}	155	GPa
	E_{22}	9.51	GPa
Shear modulus	G_{12}	5.93	GPa
	G_{23}	3.29	GPa
Poisson's ratio	ν_{12}	0.32	
	ν_{23}	0.45	
Linear thermal expansion	α_1	−1.62	μm/m°C
	α_2	30.05	μm/m°C
Density	ρ	1571.6	kg m^{-3}
Ultimate tensile strength	S_1^T	2620	MPa
	S_2^T	66	MPa
Ultimate compressive strength	S_1^C	−1620	MPa
	S_2^C	−248	MPa
Ultimate shear strength	T_{12}	103	MPa

Table 2
Mechanical properties for unidirectional lamina (0°): Carbon/Epoxy (AS4/3501-6).

Elasticity modulus	E_{11}	147	GPa
	E_{22}	10.3	GPa
Shear modulus	G_{12}	7	GPa
	G_{23}	5	GPa
Poisson's Ratio	ν_{12}	0.27	
	ν_{23}	0.02	
Linear thermal expansion	α_1	−1.62	μm/m°C
	α_2	48.6	μm/m°C
Density	ρ	1600	kg m^{-3}
Ultimate tensile strength	S_1^T	2280	MPa
	S_2^T	57	MPa
Ultimate compressive strength	S_1^C	−1725	MPa
	S_2^C	−228	MPa
Ultimate shear strength	T_{12}	76	MPa

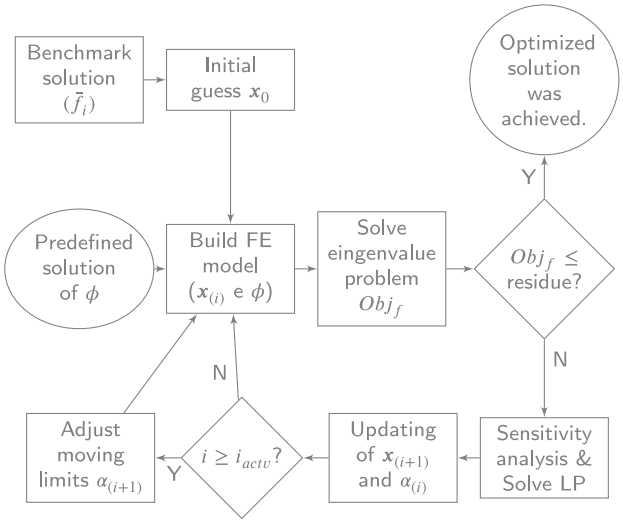

Fig. 5. Optimization flowchart.

2.2. Optimization-based repair patches

The optimization scheme adopted herein is illustrated in the flowchart of Fig. 5.

The modal response of the undamaged panels, $\bar{f}_i$, was used as input data (benchmark solution). The fiber orientation angle, ϕ, was defined as perpendicular to the damage central axis. It must be noted that despite such a strategy being extremely common and effective when applied in repairing isotropic materials such as cracked metallic components, it might not be the most efficient orientation in repairing orthotropic materials [40]. Nevertheless, in the present study, due to (i) the quasi-isotropic configuration of the parent plate and (ii) the high aspect ratio ($\approx 15:1$) of the damage region (i.e., crack-like), the fiber angle ϕ was pre-defined as perpendicular to the damage. Thus, $\phi = 0°$ was used as input for the optimization algorithm.

The initial guess x_0 for the design variables $x_{(i)}$, i.e., rectangular patch geometrical parameters, was randomly generated using the CPU time as a seed. The Finite Element (FE) model used to simulate the panels' modal response employed high-order (bi-quadratic interpolation functions) shell FE. This element type uses the first-order shear deformation theory [41], also known as Mindlin–Reissner shell theory, which applies to thin to moderately thick plates/shells [42]. Each shell FE consisted of an 8-node element with six degrees of freedom (dof) per node. The interface between the repair patch and the parent plate was assumed to be perfectly bonded. Through a mesh sensitivity analysis, the characteristic FE size, l_E, was defined with a maximum length equal to $l/50$, with l being the side length of the panels. For the damaged region's surroundings and repair patches, a mesh refinement of $1/10$ was used to better discretize the region of interest. Only quadrilateral elements formed the mesh, and the model's total number of dof varied from approximately 21 000 to 335 000; such a considerable variation is due to the possibility of the patch extending completely covering the parent plate's surface, as will be discussed at the end of the current section.

The modal analysis for determining eigenvalues and eigenvectors was performed using the block-Lanczos algorithm. The panels were assumed to be simply supported along two opposite sides, which implies constraints on all translational displacements and on roll and yaw rotations. The objective function, Obj_f, used in the optimization framework, measures the deviation in the dynamic response of the repaired structure, $\overline{f_i}$, from that of the original undamaged state, f_i. The function is evaluated over each ith vibration mode and is formulated as

$$Obj_f = \sum_{i=1}^{n} \left(\sqrt{\left(\frac{\bar{f}_i - f_i}{f_i} \right)^2} \right), \tag{1}$$

(i) Modal analysis: panels on its original state, f_i.

(ii) Inclusion of damage as controlled material removal.

(iii) Modal analysis: damaged panels, $\widetilde{f}_i$.

(iv) Shape optimization problem solution.

(v) Optimized repair patches applied to damaged panels.

(vi) Modal analysis: repaired panels, $\overline{f}_i$.

(vii) Flexural test until failure, $F_{z_{\text{ult}}}$ and $u_{z_{\text{ult}}}$.

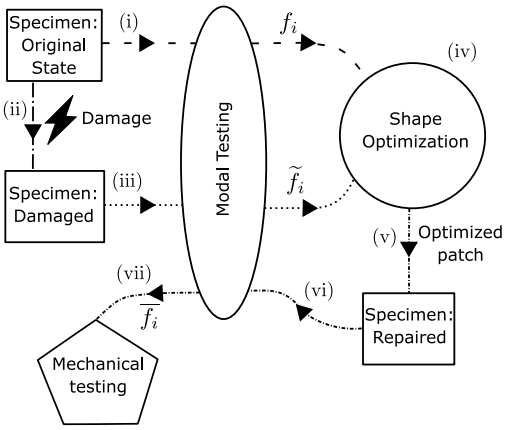

Fig. 6. Workflow adopted in the present study.

where the resulting optimization problem can be generalized as the minimization of Obj_f, as follows

$$\begin{aligned} &\underset{\boldsymbol{x}}{\text{minimize}} \quad Obj_f, \\ &\text{subjected to} \quad \boldsymbol{x}_{\min} \leq \boldsymbol{x} \leq \boldsymbol{x}_{\max}, \qquad \forall\, \boldsymbol{x} \in \Gamma_*, \end{aligned} \tag{2}$$

where the design variables $\boldsymbol{x}$ govern the shape and size of the patch, which is restricted to the feasible design domain Γ_*. In this work, Γ_* was defined to cover at least 105 % of the damage extension and, at most, the entire surface of the parent plate.

To clarify the iterative procedure that governs the evolution of the design variables, it is important to detail the Sequential Linear Programming (SLP) methodology utilized. The procedure initiates with an initial random guess for the design variables, $\mathbf{x}_0 = [l_v, l_h]^T$. Considering that the objective function is non-linear with respect to these variables, the core of the SLP method is to solve a sequence of simplified, linear subproblems [43].

In each iteration i, the following steps are performed:

i - **Linearization:** The non-linear objective function is approximated by a linear function using a first-order Taylor series expansion around the current design point, $\mathbf{x}_i$. This is achieved by computing the sensitivity of the objective function with respect to each design variable.

ii - **Moving limits:** To ensure the validity of this local linearization, 'moving limits' are employed, establishing a temporary trust region around $\mathbf{x}_i$. These limits constrain the maximum permissible alteration for each design variable within the current step and are updated at each iteration by the parameter α_i (see flowchart of Fig. 5). This parameter increases during the initial iterations where a more aggressive linearization can be assumed and decreases significantly as the solution converges towards a minimum.

iii - **LP subproblem solution:** This results in a Linear Programming (LP) subproblem, which is then solved using an interior-point algorithm to find an improved design point, $\mathbf{x}_{i+1}$. This step determines the new values for l_v and l_h.

iv - **Update and iteration:** The moving limits themselves are dynamically adjusted in subsequent iterations based on the convergence behavior, allowing for larger steps early in the process and finer adjustments as the solution approaches the optimum.

This sequence of linearization, imposing moving limits, and solving the LP subproblem is repeated until the objective function converges to a minimum value. The path taken by the design variables, as depicted in Section 3 (Fig. 10), is therefore the result of this step-by-step iterative search for the optimal solution.

2.3. Testing methodology

The workflow employed in the current study is depicted in Fig. 6. The experimental protocol comprised eight distinct stages. Initially, all ten panels in their pristine condition were assessed for their modal response to determine f_1 for each panel. Subsequently, the panels selected for damage, specifically PNL-03 to PNL-09, underwent mechanical removal of material in their central regions up to 75 % of their total thickness, as detailed in Section 2.1, with PNL-09 being a notable exception due to the complete through-thickness material removal. In their damaged state, the seven panels were subjected once more to modal testing to evaluate the modified response in terms of the first natural frequency $\widetilde{f_1}$ (damaged). The damaged panels were subsequently repaired using a patch with dimensions optimized by solving the problem detailed in Section 2.2. It is crucial to highlight that panel PNL-09 was repaired with a patch optimized for a less severe damage scenario than its actual damage state, given its extensive through-thickness material loss. The seven repaired panels were then reassessed through modal testing to evaluate the modified response concerning the first natural frequency $\overline{f_1}$ (repaired).

All modal analyses followed the same testing protocol. The panels were excited using an instrumented impact hammer, and the response signal was retrieved via a piezoelectric accelerometer. Data acquisition and processing were performed using the four-channel Saturn SD380-C7 system. The impact hammer (Kistler 9724A2000) was configured according to the manufacturer's recommendations, utilizing an SF10-SS super-soft rubber tip, a rubber tip adapter, and an additional 125.0 g mass. It operates within a force range of up to 2.0 kN, with a sensitivity of 2.0 mV N^{-1} and a resonance frequency of 27.0 kHz. The accelerometer (PCB352C33) had a total mass of 14.5 g a frequency range of 0.5 Hz to 10.0 kHz, a sensitivity of 10.2 mV/(m/s^2), and a resonance frequency above 50.0 kHz. It was attached to the panels using beeswax, with measurements taken at two distinct positions per panel. The Saturn SD380-C system was set to a response range of 0.0 Hz to 200.0 Hz, covering the estimated natural frequencies from previous finite element simulations. It operates within 0.0 Vrms to 20.0 Vrms, with a sampling rate of up to 51.2 kHz. A gain of 0.1 V V^{-1} was applied to the hammer signal and 10.0 V V^{-1} to the accelerometer signal. Fig. 7 illustrates the equipment described herein.

Each panel was tested with the accelerometer in two positions (SA and SC) and subjected to impact at three locations (#1, #2, and #3) sequentially, as illustrated in Fig. 8(a). The modal response was obtained as the average of the signals from both sensor positions. Each impact-generated response was processed through a Fast Fourier Transform (FFT) to compute the panel's frequency response spectrum.

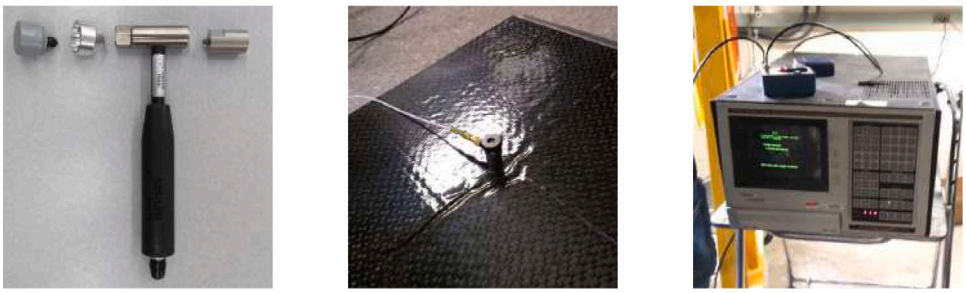

(a) Impact hammer. (b) Piezoelectric accelerometer (c) Data acquisition system.

Fig. 7. Experimental apparatus used in modal analyses.

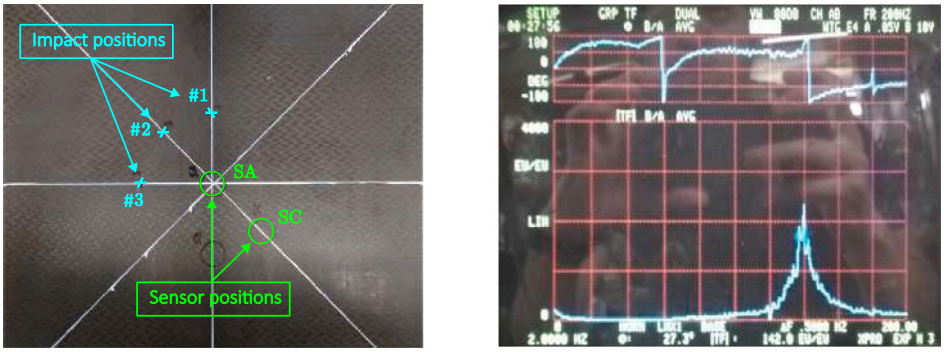

(a) Sensors positioning. (b) Typical response signal.

Fig. 8. Setup details of the modal analyses.

A typical response signal is shown in Fig. 8(b), where the lower graph represents the natural frequency vs. signal amplitude, while the upper graph displays the phase angle response. Since modal displacement analysis was not the focus of this study, only the natural frequency peaks were extracted.

The restoration of the damaged panels involved a multi-step repair protocol. Initially, the surfaces of the damaged region were prepared for adhesive application by cleaning them thoroughly with acetone (96.4%), followed by isopropyl alcohol (99.9%) to eliminate any contaminants. The region of the substrate panel designated for the repair patch underwent light sanding (120 grit) to introduce abrasion-induced roughness on the bonding surface. Subsequently, the void resulting from mechanical material removal was filled with carbon fiber scraps (short fibers) as a filler, ensuring a level surface for the ensuing patch application. The repair patch was applied through a wet layup method. The AS4 carbon fiber fabric was precisely cut to the optimized dimensions with an additional margin to facilitate handling, trimmed subsequent to application. The fabric was then fully impregnated with a West System 105/209 epoxy resin system [38], which functioned as both the matrix for the patch and the adhesive bonding it (following resin application post-vacuum degasification) to the parent panel in a single operation. The patch was applied uncured to the prepared surface.

The curing process proceeded in two stages under constant pressure. A weight of approximately 2.7 kg was placed over the repaired region, with wax paper set between the weight and the patch to ensure a uniform surface finish and prevent undesirable adhesion. The initial curing phase occurred at ambient temperature (25.0 °C) for a duration of eight hours. This was followed by a post-curing phase executed in an oven at a controlled temperature of 45.0 °C for an additional 16 h to ensure complete polymerization of the resin. The procedure adhered to established best practice protocols from prior research conducted at the Polymer Technology Center (PTC) at Texas A&M University.

The mechanical tests until failure were conducted using a three-point bending fixture (ASTM D790 [44]) mounted on a servo-hydraulic universal testing machine (MTS 810) with a maximum load capacity of 244.0 kN. Due to the panel dimensions, strict adherence to standard testing guidelines was not feasible. Instead, the best possible arrangement was sought to ensure proper positioning relative to the supports (Fig. 9(c)) and the loading knife (Fig. 9(b)). The knife edge was placed at the center of gravity of the panels, aligned transversely to the bonded patches, while the supports were positioned past the patch edges. Fig. 9(a) illustrates the adopted setup, ensuring that the repair region was subjected to direct loading without overlapping the supports or the patch edges. The total span between supports was 203.2 mm, and both the knife edge and supports had a depth of 50.8 mm. Details of the test setup are provided in Fig. 9.

The three-point bending tests were executed utilizing a singular test setup. To assess the performance of repairs under different loading conditions, the specimens were tested in two distinct orientations. In the initial orientation, a portion of the repaired panels were tested with the patched surface oriented upwards, thereby subjecting it to a condition of maximum bending stress with the patch experiencing nominal compression. Conversely, in the second orientation, the remaining panels were tested in an inverted manner, with the patched surface facing downwards, thus exposing it to maximum bending stress with the patch under nominal tension. While it is acknowledged that the three-point bending tests and the panel configuration result in a complex multi-axial stress state, manifested by the anticlastic effect (a result of the Poisson effect), this methodology permits a direct evaluation of the patch's efficacy when the predominant stress on its surface is either tensile or compressive.

All tests were performed at room temperature of 23.0 °C, and specimens were bent until failure. The stopping criterion was abrupt panel failure, identifiable by rupture at the contact region with the knife edge and a sudden drop in the force–displacement curve. The ultimate force

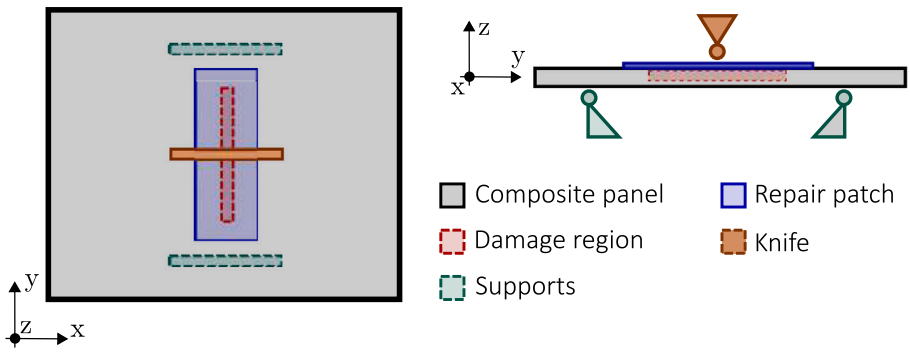

(a) 3-points bending setup for the repair patch under nominal compression.

(b) Panels top surface.

(c) Panels bottom surface.

Fig. 9. Mechanical testing until failure.

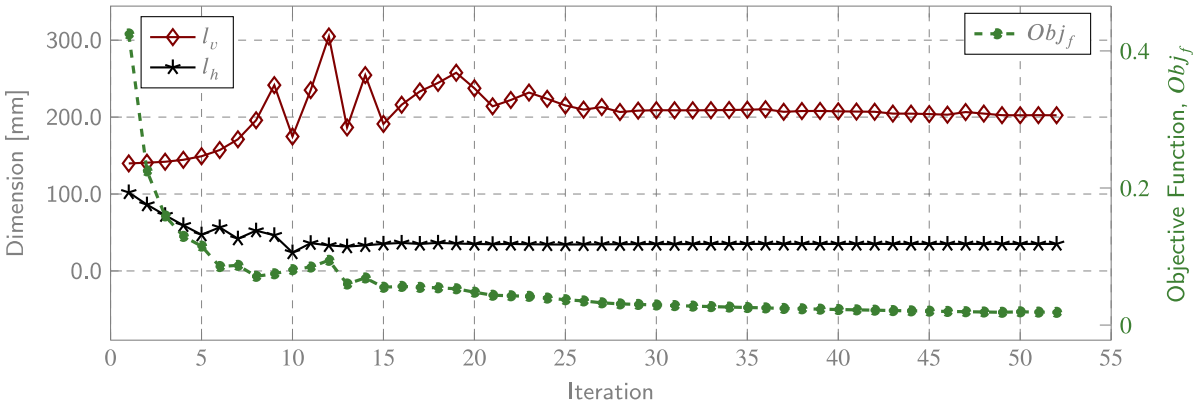

Fig. 10. Convergence of design variables (l_v, l_h) and the objective function (Obj_f) during the optimization process.

(F^z_{ult}) and failure displacement (u^z_{ult}) were recorded at the moment just before failure.

The bending tests were conducted at a constant displacement rate of 6.4 mm/min, a typical value for composite testing. However, for specimens PNL-06 and PNL-09, a lower rate of 2.5 mm/min was used to investigate whether increased sensitivity could capture fiber rupture events during loading. No significant differences were observed.

3. Results

The optimization analysis was carried out by evaluating the first natural frequency of the panel under various conditions, including pristine, damaged, and repaired states. As a result, the objective function, referenced in Eq. (1), was reformulated as indicated in

$$Obj_f = \sum\left(\sqrt{\left(\frac{\bar{f}_1 - f_1}{f_1}\right)^2}\right). \tag{3}$$

The optimization problem used 145.3 Hz as the reference average for f_1, which was experimentally assessed through the modal tests of the pristine panels PNL-00, PNL-01, and PNL-02, as detailed in Section 2.3. Furthermore, assuming a rectangular repair patch reduces the design vector to two variables: the dimensions comprising the side lengths l_v and l_h. This consideration facilitated the formulation of the optimization problem, integrating these design dimensions into Eq. (2). Fig. 10 illustrates the solution associated with this optimization problem. The objective function Obj_f evolution across iterations is shown on the right vertical axis, while the convergence of the design variables l_v and l_h is depicted on the left vertical axis.

The convergence criterion was met after 52 iterations. The total computational time amounted to 509.6 s, with only 206.5 s spent on the actual optimization; the residual time was devoted to the iterative analysis of the resulting FE models during each iteration i. The optimal configuration corresponded to a rectangular patch with dimensions l_v = 202.4 mm by l_h = 35.1 mm, yielding a total area of 7101.5 mm^2. Comparatively, the single-layer repair patch's total area constituted 7.6 % of the panel's total surface area, and was 5.4 times larger than the damaged region's surface area.

Using the optimized configuration for the single-layer repair patch, seven patches were cut from the AS4 carbon fiber fabric, which were

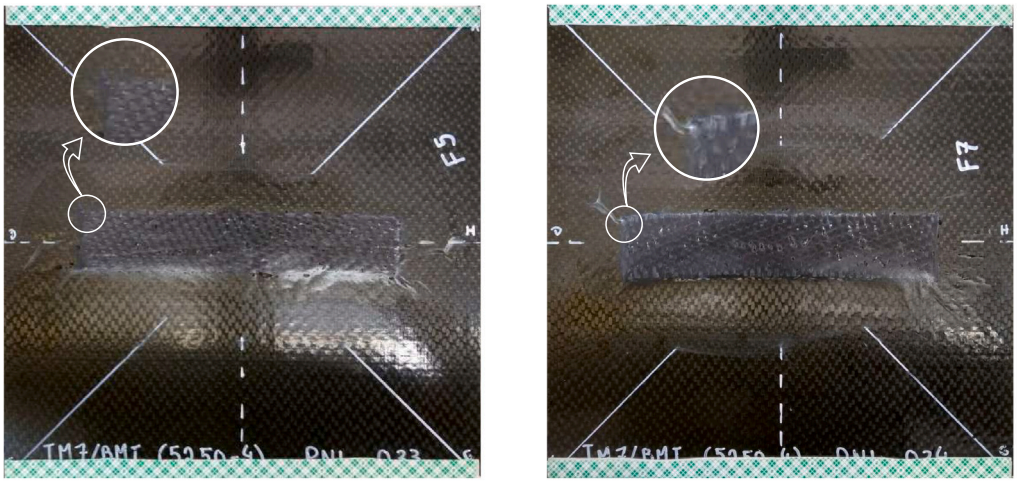

(a) PNL-03 repaired. (b) PNL-09 repaired.

Fig. 11. Specimens repaired with optimized patches.

Table 3
Modal test results: damaged panels.

Specimen	$\widetilde{f_1}$[Hz]		Avg.	Dispersion
	Sensor SA	Sensor SC	[Hz]	
PNL-03[a]	123.82	–	123.8	−0.5
PNL-04	135.25	133.36	134.3	0.8
PNL-05	134.33	133.63	134.0	0.8
PNL-06	134.45	136.63	135.5	1.0
PNL-07	116.05	110.38	113.2	−1.8
PNL-08	128.72	130.15	129.4	0.2
PNL-09[b]	119.14	125.95	122.5	−0.6

[a] Corrupted data for the sensor SC resulted in the loss of such result.
[b] Through-thickness damage.

Table 4
Modal test results: repaired panels.

Specimen	$\overline{f_1}$[Hz]		Avg.	Dispersion
	Sensor SA	Sensor SC	[Hz]	
PNL-03	139.28	141.61	140.4	−0.7
PNL-04	142.89	145.08	145.1	0.8
PNL-05	140.75	143.43	142.1	−0.2
PNL-06	144.46	146.80	145.6	1.0
PNL-07	146.36	145.99	146.2	1.2
PNL-08	138.06	138.43	138.2	−1.5
PNL-09[a]	140.57	141.52	141.0	−0.5

[a] Through-thickness damage.

used to restore the damaged panels PNL-03 to PNL-09. Fig. 11 presents the final configuration of two distinct repaired panels. Figs. 11(a) and 11(b) offer an enlarged detail view to illustrate the fabric pattern of the repair layer after full curing.

3.1. Modal response analysis

Following the infliction of damage, the panels were subjected to modal testing to determine the reduction in stiffness resulting from material removal. The outcomes of these tests are depicted in Table 3, which outlines changes in the first natural frequency $\widetilde{f_1}$. It is noteworthy that for PNL-03, the reported findings in regard to $\widetilde{f_1}$ are limited to sensor SA due to data loss caused by the corrupted signal from sensor SC. It also should be highlighted that the dispersion measure was calculated as the number of standard deviations (SDs) by which the computed average deviated from the benchmark value of f_1. The first natural frequency of vibration for the pristine panels, f_1, was 145.3 Hz, closely matching the finite element (FE) simulations. Detailed information regarding the FE model formulation and mesh convergence analysis is provided in Appendix. In contrast, the average modal response for the damaged specimens was 127.6 Hz, indicating a 12% reduction in the first vibration mode due to damage. This deviation slightly exceeds the expected numerical predictions, likely due to the inclusion of the most critical through-thickness damage case in the dataset. The standard deviation for the damaged panels was 8.2 Hz, and within a 95% confidence interval (±2 SDs), no specimen exhibited outlier behavior. Overall, minimal discrepancies ($\lesssim 1.5\%$) were observed between measurements taken at SA and SC sensor positions, except for PNL-09, which exhibited a 5.3% difference. Theoretically, peak frequency measurements should remain identical, regardless of sensor position, with only amplitude and phase variations. However, due to the presence of a through-thickness damage region in PNL-09, standard placement of the SA sensor (as shown in Fig. 8(a)) was not possible. As a result, the sensor had to be positioned near the edge of the oblong perforation, potentially compromising the quality of the coupling and introducing measurement discrepancies.

After repair, the panels were subjected to an additional series of modal tests to assess improvements in their first natural frequency response. The findings from these tests, conducted on specimens PNL-03 through PNL-09 in their restored condition, are compiled in Table 4.

The analysis of the first natural frequency for the repaired panels, as shown in $\overline{f_1}$, yielded an average value of 142.7 Hz, which corresponds to a restoration efficiency of 98.2% with respect to the undamaged benchmark frequency $f_1 = 145.3$ Hz. The calculated standard deviation was 3.0 Hz, and no statistical outliers were detected within a 95% confidence interval (±2 SDs). These findings corroborate the substantial efficacy of the restoration process. Fig. 12 compares the modal results for the repaired panels, assessed in terms of $\widetilde{f_1}$ (refer to Table 4), relative to the modal response of the panels in their damaged condition, represented in terms of $\overline{f_1}$. Additionally, the benchmark solution, $f_1 = 145.3$ Hz, obtained for panels in their pristine form, is also included.

These results demonstrate consistency across the analyzed scenarios, especially regarding the first natural frequency of the repaired panels ($\overline{f_1}$), which exhibited a standard deviation of 3.0 Hz. Among the specimens, PNL-07 deviated the most from the sample mean, with its response lying $-1.8 \times$ SDs below average. Still, this value remained within the 95% confidence interval, reinforcing the uniformity of the

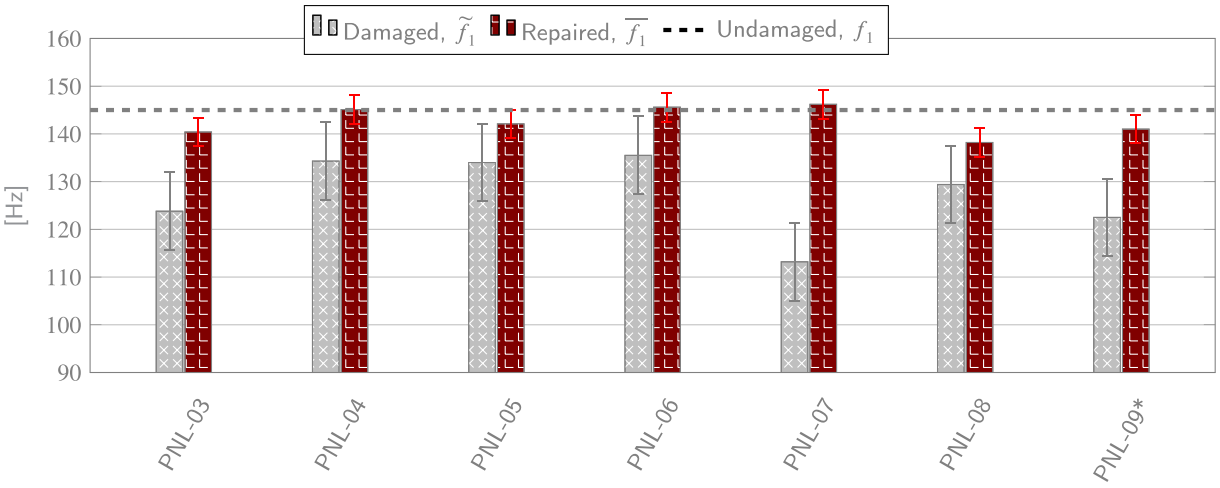

Fig. 12. Panels modal response: damaged and repaired.

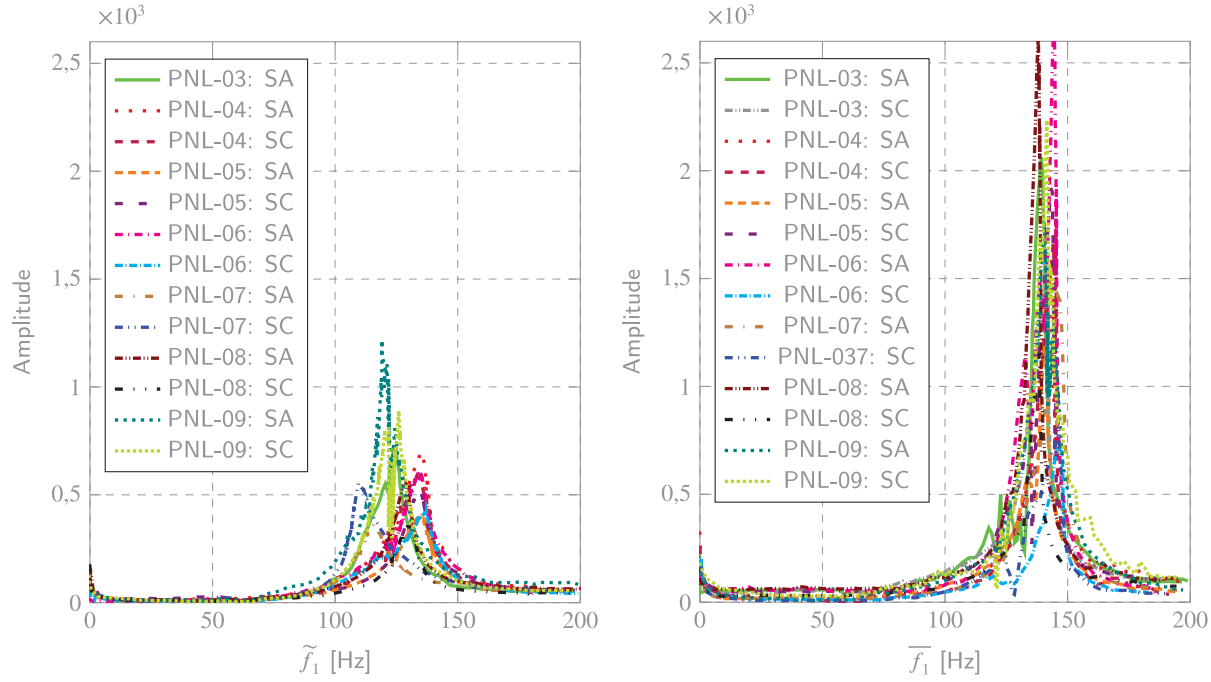

(a) Modal response curves: damaged specimen.

(b) Modal response: repaired specimen.

Fig. 13. Modal response for all panels, damaged and repaired, at two distinct sensor positions: SA and SC.

restoration process. Fig. 12 also highlights an interesting observation regarding PNL-09. Although it underwent the most severe damage – a through-thickness material removal – its restoration efficiency remained comparable to that of the other specimens. This suggests that, despite the patches being optimized for a different configuration, the repair methodology was effective in recovering stiffness. However, as will be discussed in the following section, such efficiency is less evident when evaluating mechanical resistance through three-point bending tests.

Fig. 13 illustrates the modal response curves for each panel before and after repair, overlaid for direct comparison. Significant variations in signal amplitude among specimens are anticipated due to the nature of the test. The introduction of damage inherently induces greater dispersion of the signal curves about the average $\widetilde{f_1}$, Fig. 13(a). Nevertheless, the repair procedure effectively consolidates the curves, thereby reducing the dispersion around the average response as noted in $\overline{f_1}$, Fig. 13(b).

3.2. Three-point bending tests

For an initial assessment of the repair's effectiveness in restoring the ultimate load capacity, a three-point bending test was selected. This test facilitates the experimental protocol for multiple specimens and allows for the straightforward evaluation of the patch under both nominal tension and compression by simply inverting the panel. Although it is recognized that the three-point bending test is not designed to capture complex damage initiation and progression, it remains a reliable method for verifying the final failure behavior and the overall structural integrity of the repaired panels.

A critical aspect for interpreting the ultimate load results is the qualitative analysis of the failure modes. The undamaged (pristine) specimens consistently exhibited a catastrophic failure mode, characterized by extensive fiber breakage on the tensile bottom surface and compressive crushing near the central loading point (close to the knife).

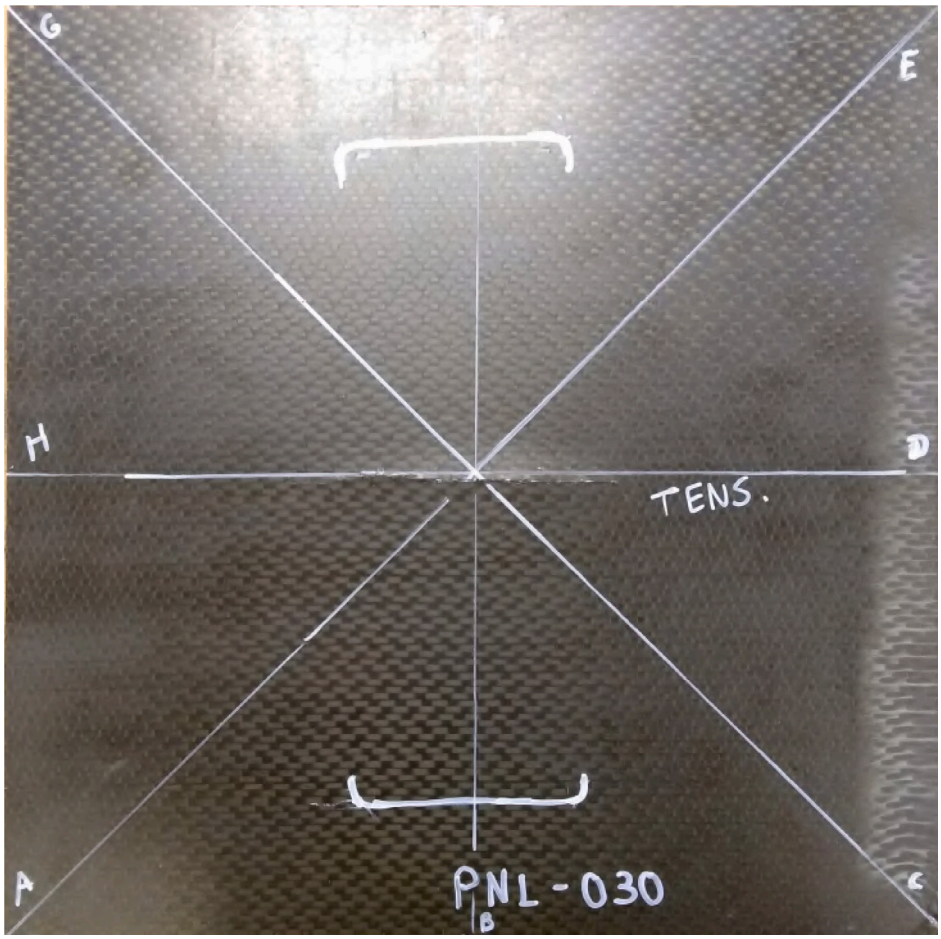

Fig. 14. Representative failure of a repaired panel (PNL-03) after the bending test, depicting a through-thickness crack in its central region.

This manifested as a crack-like line across the panel's width, a behavior that is representatively illustrated for a repaired panel in Fig. 14.

Notably, the repaired specimens exhibited an almost identical failure mechanism. Failure consistently propagated through the thickness (trespassing crack) of the parent laminate, reflecting the behavior observed in the pristine panels. During the loading phase, audible emissions frequently signified the initiation of internal damage, culminating in a sudden and final rupture.

Of critical importance, in all repaired specimens, the failure was dictated by the structural limitations of the parent laminate rather than the repair itself. As illustrated in the detailed views in Fig. 15, there was an absence of premature patch debonding, peeling, or adhesive failure at the patch boundaries. This observation confirms that the optimized patch effectively transferred the load without introducing a new, weaker failure pathway. This qualitative consistency provides essential context for validating the quantitative results summarized in Table 5. Future investigations could involve in-plane shear tests to further examine the interlaminar stress states, particularly regarding repairs on thicker laminates. It is important to note that the aspect ratio for the tested panels was $\approx 78 \times 1$.

The summarized results of the bending tests are presented in Table 5. All ten specimens were tested to failure: three in their pristine, undamaged condition (PNL-00, PNL-01, and PNL-02) and seven panels repaired with optimized rectangular patches (PNL-03 to PNL-09) (202.4 mm × 35.1 mm). In terms of loading orientation, PNL-03 and PNL-04 were tested with the patch side under nominal compression, whereas the remaining panels were assessed under nominal tension.

The undamaged panels exhibited a remarkable consistency in both maximum load-bearing capacity and failure displacement. In contrast, the repaired panels demonstrated greater variability; nevertheless, their mechanical performance proved consistent regardless of whether the patch experienced nominal compressive or nominal tensile loading. This variability is attributed to the manual nature of patch application, which inherently limits repeatability. Notably, specimen PNL-07 exhibited significantly inferior performance relative to the others, especially in terms of ultimate load (F_z^{ult}), and this anomaly will be addressed in the ensuing paragraphs. Overall, the optimized patches functioned efficiently, restoring approximately 94% of the original load capacity on average. This result is noteworthy given that: (i) the patches were exclusively optimized for the modal response rather than for static load-bearing strength; and (ii) the severity of the damage incurred. Fig. 16 illustrates a bar chart summarizing these findings: the undamaged panels achieved an average $F_z^{\text{ult}} = -8936.5$ N (SD = 241.6 N), whereas the repaired panels attained an average of −8393.9 N.

Table 5
Summary of three-point bending test results.

Specimen	Patch nominal stress state:	$\dot{u}$ [mm/min]	F_z^{ult} [N]	u_z^{ult} [mm]
PNL-00	–	6.35	−8810.36	−25.33
PNL-01	–	6.35	−8783.97	−25.10
PNL-02	–	6.35	−9215.02	−25.21
PNL-03	Compression	6.35	−8278.29	−24.32
PNL-04	Compression	6.35	−8491.68	−24.51
PNL-05	Tension	6.35	−8174.30	−22.91
PNL-06	Tension	2.54	−8504.19	−25.39
PNL-07	Tension	6.35	−7659.66	−23.16
PNL-08	Tension	6.35	−8821.79	−23.71
PNL-09[a]	Tension	2.54	−8827.16	−26.31

[a] Through-thickness damage.

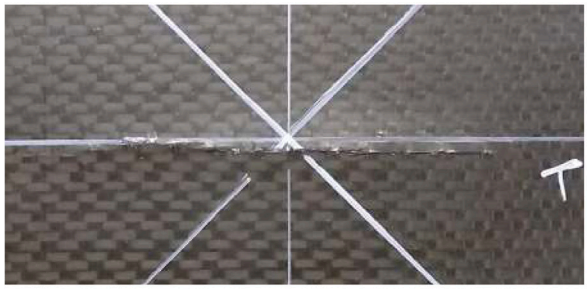

(a) PNL-00: panel fracture, bottom view.

(b) PNL-05: panel fracture, top view.

(c) PNL-06: panel fracture, top view.

(d) PNL-09*: panel fracture, bottom view.

Fig. 15. Representative failure modes observed in pristine and repaired specimens.

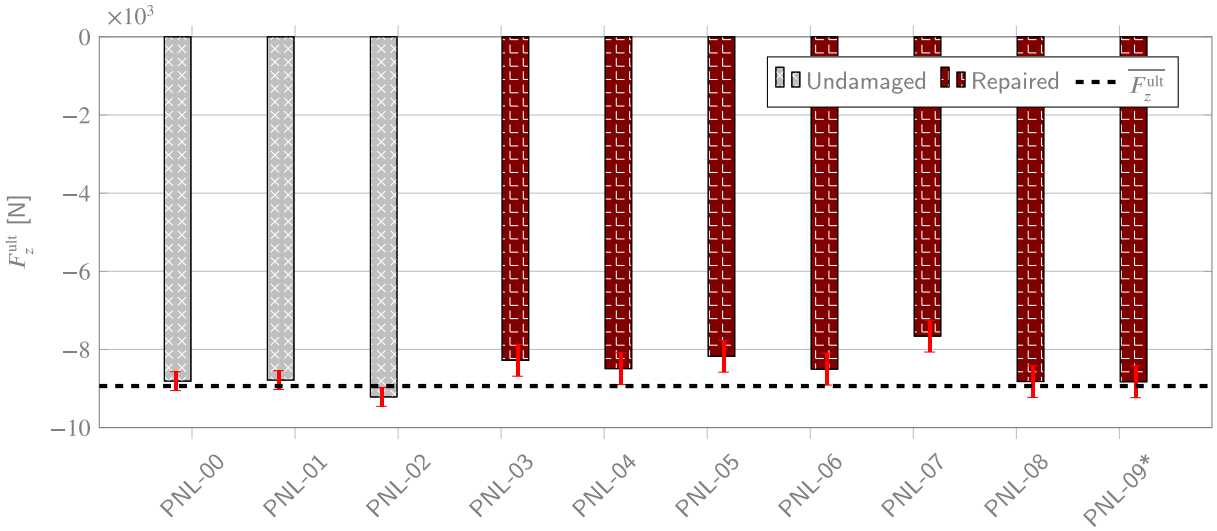

Fig. 16. Three-point bending: ultimate load (F_z^{ult}).

The ultimate displacement of the undamaged and repaired panels are presented in Fig. 17. The undamaged panels exhibited an average ultimate displacement (u_z^{ult}) of −25.2 mm, with a sample standard deviation of 0.1 mm. In comparison, the repaired panels showed a slightly lower average of −24.3 mm and a substantially higher standard deviation of 1.2 mm, approximately 11 times greater. However, this contrast stems from the exceptionally low dispersion among the undamaged specimens, indicating strong population representation. When evaluated in relative terms, this difference becomes even more evident, as shown in Table 6.

Using a 2 × SDs confidence interval, panel PNL-07 was the only specimen to exhibit a statistically atypical response, with a deviation of −3.14×SDs from the mean F_z^{ult}, corresponding to a −14.29% deviation—strongly indicative of an outlier. Interestingly, its ultimate displacement deviated much less from the average. It is worth noting that PNL-07 had already shown a −1.8 × SDs deviation in modal response when damaged, as previously discussed. Overall, as illustrated in the box plots of Fig. 18, the dispersion in both F_z^{ult} and u_z^{ult} remained statistically comparable across specimens.

As shown in Fig. 18(a), the peak load sustained by the repaired panels was consistently lower than that of the undamaged ones. Conversely, Fig. 18(b) shows that the ultimate displacement of the repaired panels fluctuated around the undamaged mean, suggesting that, on average, the original flexibility was nearly restored — an outcome aligned with the observed recovery in modal response (f_1). Meanwhile, the monotonic trend in F_z^{ult} confirms that although the optimized patches enhanced structural strength, full recovery to the original performance level was not achieved. Notably, a significant portion of the variability within the repaired group can be attributed to panel PNL-09, which exhibited a through-thickness defect – a more critical condition not addressed in the patch design – resulting in a more compliant repaired configuration.

Fig. 19 demonstrates a comparative analysis of a pristine panel and a repaired one, both subjected to bending until failure, in terms

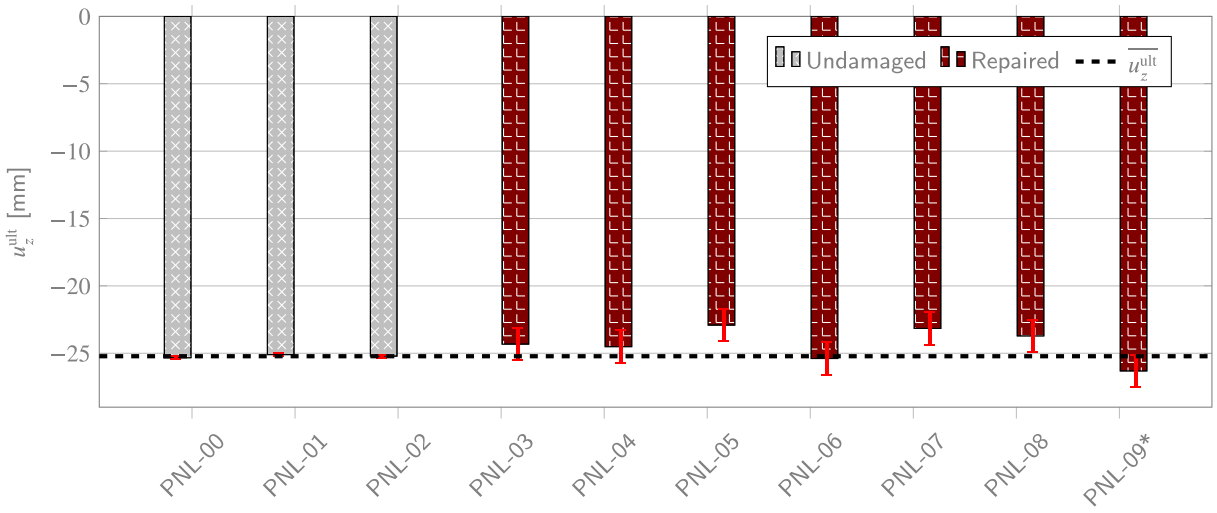

Fig. 17. Three-point bending: ultimate displacement (u_z^{ult}).

Table 6
Results dispersion — repaired panels (three-point bending).

Especimen	Max. Load	Displacement	Percentile difference		Dispersion (SD)	
	$F_{z_{ult}}$[N]	$u_{z_{ult}}$[mm]	$\overline{F_z^{ult}}$	$\overline{u_z^{ult}}$	$\overline{F_z^{ult}}$	$\overline{u_z^{ult}}$
PNL-03	−8278.29	−24.32	−7.36	−3.54	−1.62	−0.73
PNL-04	−8491.68	−24.51	−4.98	−2.80	−1.09	−0.58
PNL-05	−8174.30	−22.91	−8.53	−9.15	−1.87	−1.90
PNL-06	−8504.19	−25.39	−4.84	0.71	−1.06	0.15
PNL-07	−7659.66	−23.16	−14.29	−8.15	−3.14	−1.69
PNL-08	−8821.79	−23.71	−1.28	−5.98	−0.28	−1.24
PNL-09[a]	−8827.16	−26.31	−1.22	4.33	−0.27	0.90

[a] Through-thickness damage.

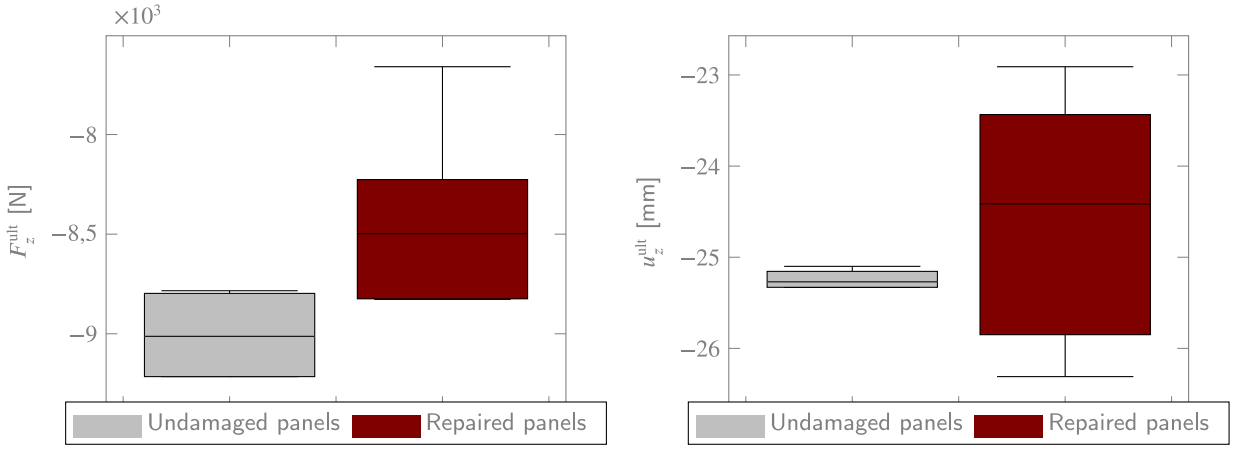

(a) Box plot: F_z^{ult}.

(b) Box plot: u_z^{ult}.

Fig. 18. Results dispersion for the undamaged and repaired configurations.

of force versus displacement. The analogous slope of the curves in Fig. 19 effectively demonstrates the efficacy of the optimized patches in reinstating the mechanical response of the panels to their original condition. In this graph, both curves are truncated at the point of abrupt failure, delineating both F_z^{ult} and u_z^{ult}.

It is particularly noteworthy that the patches, which were optimized solely based on a dynamic criterion (restoring the first natural frequency), also demonstrated excellent performance in the static three-point bending tests, recovering on average 94% of the original load capacity. This result suggests that a modal-based optimization approach, by holistically accounting for the stiffness-to-mass ratio, can serve as an effective strategy for restoring the overall mechanical performance of a repaired component, not just its dynamic behavior.

4. Conclusions

This work introduced a novel methodology for optimizing the geometry of fiber-reinforced bonded patches, addressing key limitations of conventional design approaches. By utilizing a shape-parameter-based optimization framework centered on the first natural frequency, this strategy moves beyond traditional stiffness or stress-based criteria. In contrast to these prevalent methods, the formulation proposed

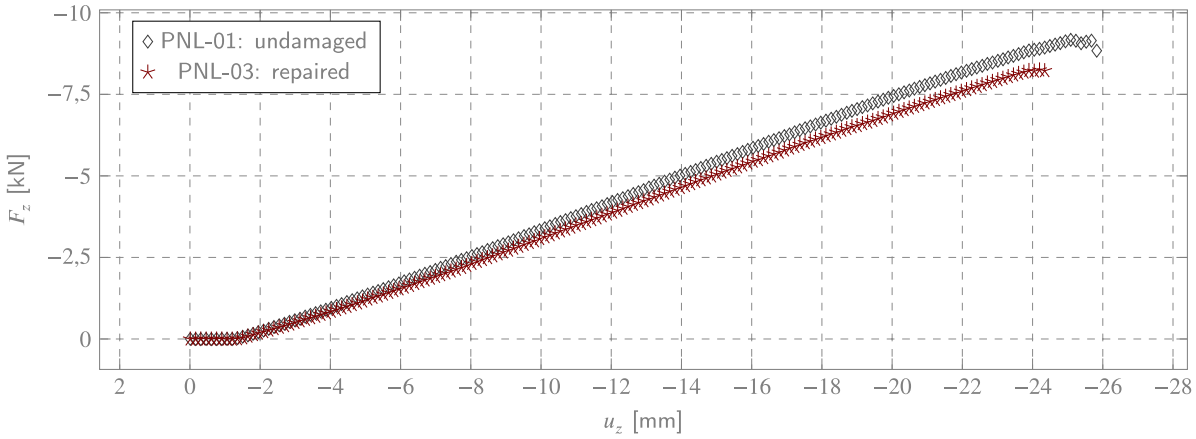

Fig. 19. Force versus displacement curves - three-points bending.

herein inherently incorporates structural inertia, facilitating a more comprehensive optimization process that is critical for aerospace components sensitive to dynamic loads. Notably, the methodology was applied to simple, field-applicable geometries (rectangular and elliptical[1]), thereby bridging the gap between theoretically complex shapes encountered in the literature and the practical MRO needs.

The optimized patch configuration was effectively implemented on IM7/BMI laminated panels in accordance with a comprehensive application protocol. A principal finding of this investigation is that patches optimized exclusively based on a dynamic criterion (modal restoration) also exhibited commendable performance in static assessments. The repairs effectively reinstated both dynamic and static responses: the first natural frequency was recovered to 98.2% of its original value, while the maximum load and displacement at failure reached 94.0% and 96.5%, respectively. This significant outcome indicates that modal-based optimization, by comprehensively considering the stiffness-to-mass ratio, can serve as a highly efficacious and versatile design strategy. Furthermore, the observed failure modes confirmed the robustness of the repair. The failure behavior of the repaired panels remained consistent with that of the undamaged specimens, showing no evidence of collateral damage, premature debonding, or adhesive failure. This confirms the effectiveness of the patching strategy in restoring structural integrity without introducing new failure mechanisms.

This study, which primarily concentrated on modal and static restoration, establishes a solid groundwork for addressing the principal challenges associated with composite repair and may be extended to explore fatigue life restoration in the future. Furthermore, the development of a robust optimization framework for practical patch geometries marks an essential step towards cultivating the engineering confidence necessary for the ultimate certification of exclusively adhesively bonded repairs on primary aerostructures.

CRediT authorship contribution statement

Leonel Echer: Writing – original draft, Visualization, Validation, Software, Methodology, Investigation, Formal analysis, Conceptualization. **Ozden O. Ochoa:** Writing – review & editing, Supervision, Conceptualization. **Carlos Eduardo de Souza:** Writing – review & editing, Software, Methodology. **Rogério J. Marczak:** Writing – review & editing, Supervision, Resources, Project administration, Funding acquisition.

[1] Although the algorithm was applied to rectangular patches, it is also compatible with elliptical base geometries.

Declaration of competing interest

The authors declare the following financial interests/personal relationships which may be considered as potential competing interests: Leonel Echer reports financial support was provided by Coordination for the Improvement of Higher Education Personnel. Rogério José Marczak reports financial support was provided by National Council for Scientific and Technological Development. If there are other authors, they declare that they have no known competing financial interests or personal relationships that could have appeared to influence the work reported in this paper.

Acknowledgments

The authors gratefully acknowledge the financial support from the Brazilian research agencies CAPES (Coordination for the Improvement of Higher Education Personnel) and CNPq (National Council for Scientific and Technological Development), grants no. 431586/2016-0 and 310649/2017-0. The authors also wish to thank *Lockheed Martin Aeronautics* (Fort Worth, TX, USA) for the generous donation of the IM7/BMI panels used in this study. Sincere appreciation is extended to Professors Carlos R. Corleto, Harry A. Hogan, and Terry Creasy for their invaluable guidance and insightful discussions during the research period at Texas A&M University (TAMU). This work forms part of a Ph.D. study conducted at the Federal University of Rio Grande do Sul (UFRGS), Brazil, with a collaborative period at TAMU, USA; the support from both institutions is greatly appreciated.

Appendix. Supplementary information on the finite element models

This appendix provides additional details regarding the finite element models employed in this study, specifically focusing on the panel and patch modeling, mesh characteristics, and the full set of numerically obtained modal responses for the different structural configurations. The models were formulated following the methodology and boundary conditions detailed in Section 2.2, utilizing the constitutive properties presented in Tables 1 and 2.

A.1. Laminated panel and patch modeling

Representative FE models illustrating the pristine, damaged, and repaired configurations are presented in Figs. 20 to 22. Note that, since all models employed shell FE, the three-dimensional thickness effect shown in these figures is purely illustrative. Moreover, the finite element mesh density exemplifies the characteristic element size derived from sensitivity analysis, as detailed in Section 2.2.

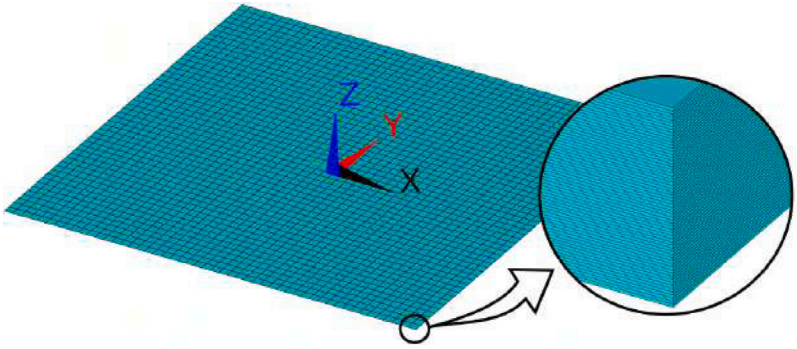

Fig. 20. Finite element model of a pristine (undamaged) panel.

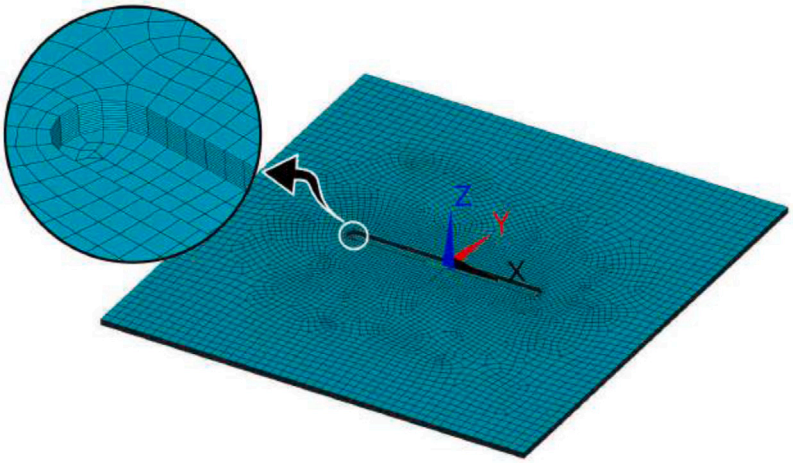

Fig. 21. Finite element model of a damaged panel, highlighting the partial-thickness material removal region.

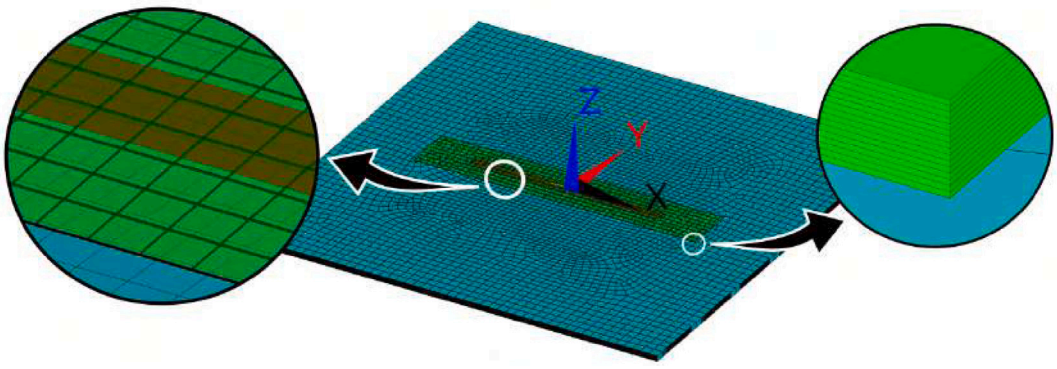

Fig. 22. Finite element model of a repaired panel, illustrating the laminate, filler, and patch materials.

A.2. Simulated modal responses

The simulated modal responses for the first three vibration modes, derived from the validated finite element models, are presented below for the pristine (Figs. 23 to 25), damaged (Figs. 26 to 28), and repaired (Figs. 29 to 31) configurations. These contour plots visually confirm the changes in modal shapes induced by the damage and demonstrate the effectiveness of the optimized repair in restoring the original dynamic characteristics.

Data availability

Data will be made available on request.

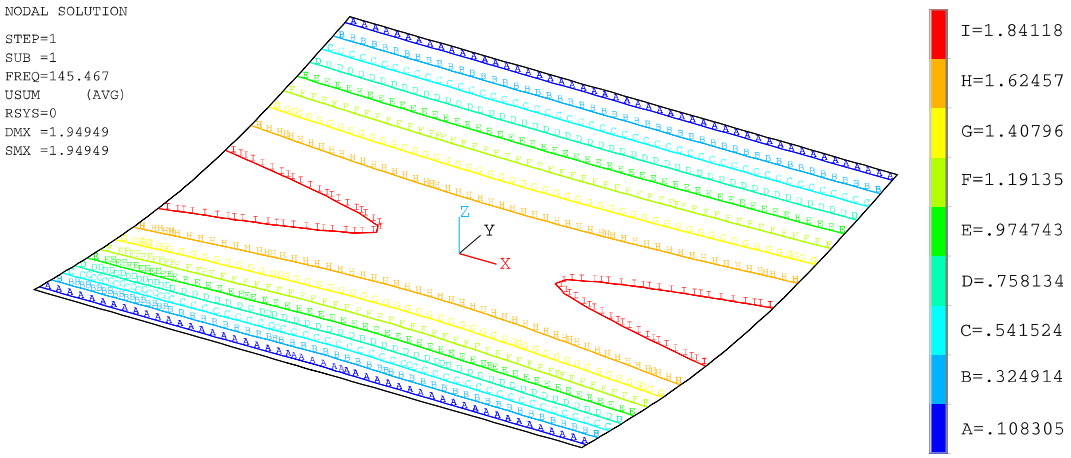

Fig. 23. Simulated modal response for the pristine panel: first mode, $f_1 = 145.5$ Hz.

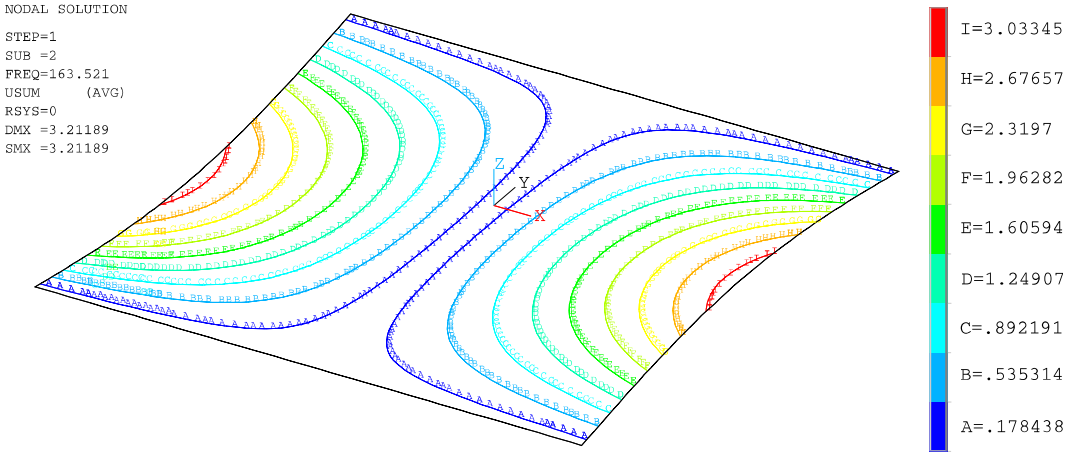

Fig. 24. Simulated modal response for the pristine panel: second mode, $f_2 = 163.5$ Hz.

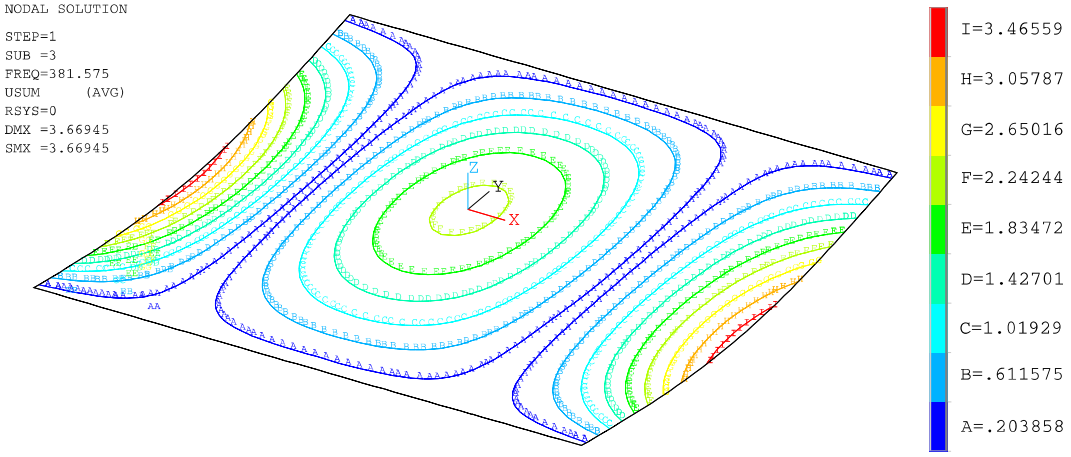

Fig. 25. Simulated modal response for the pristine panel: third mode, $f_3 = 381.6$ Hz.

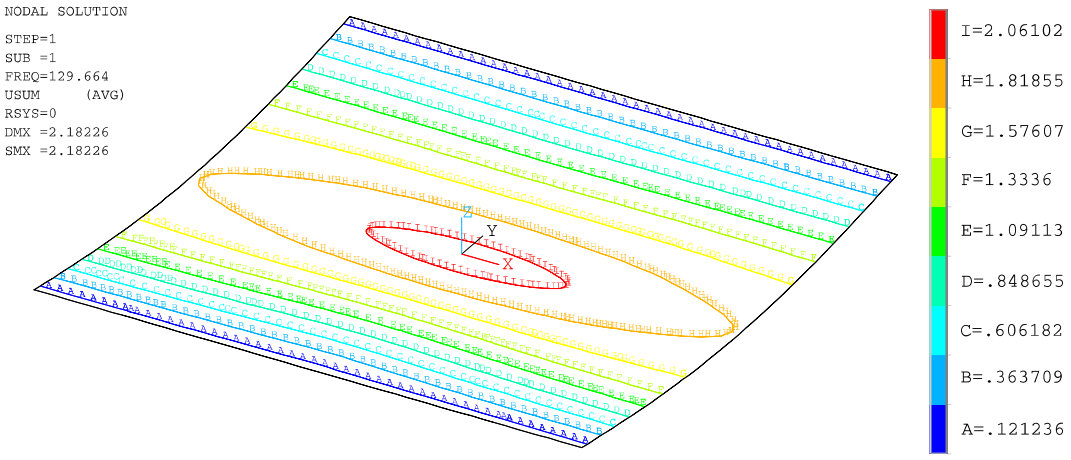

Fig. 26. Simulated modal response for the damaged panel: first mode, $\widetilde{f}_1 = 129.7$ Hz.

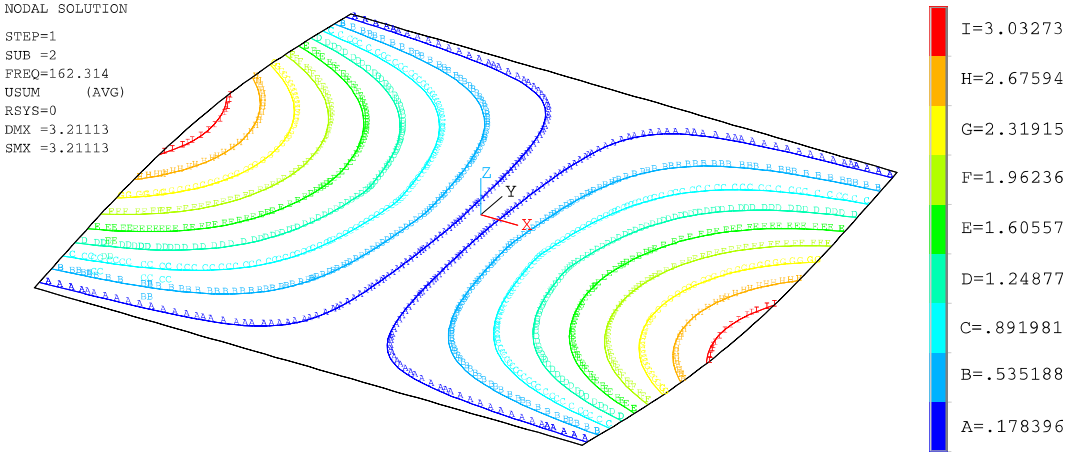

Fig. 27. Simulated modal response for the damaged panel: second mode, $\widetilde{f}_2 = 162.3$ Hz.

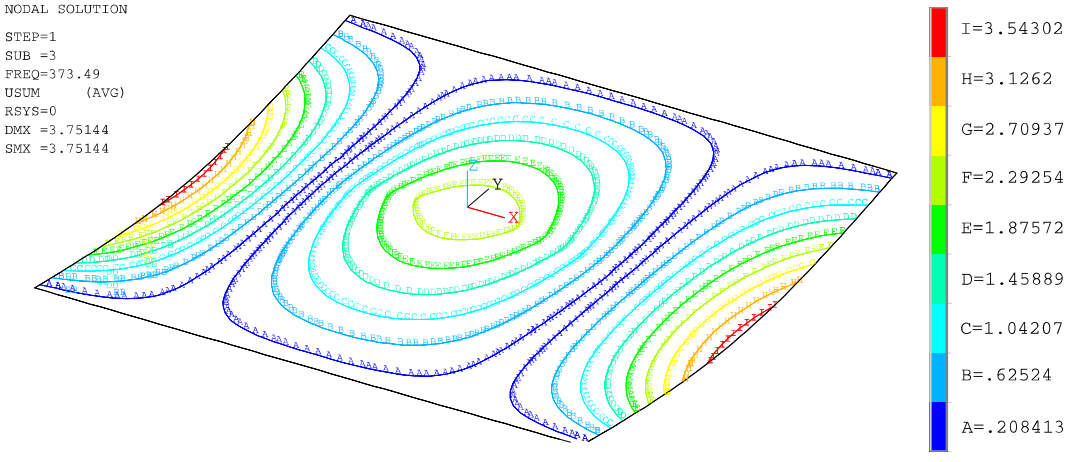

Fig. 28. Simulated modal response for the damaged panel: third mode, $\widetilde{f}_3 = 373.5$ Hz.

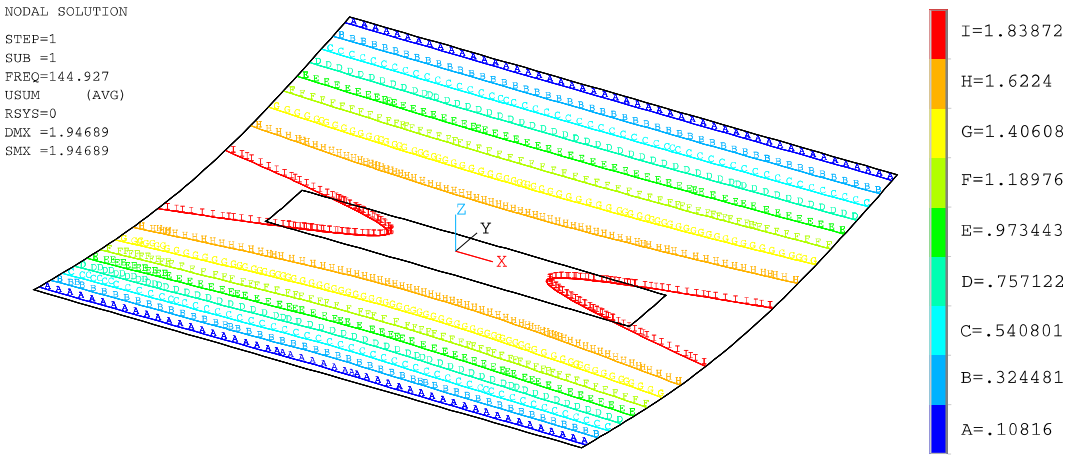

Fig. 29. Simulated modal response for the repaired panel: first mode, $\overline{f_1} = 144.9$ Hz.

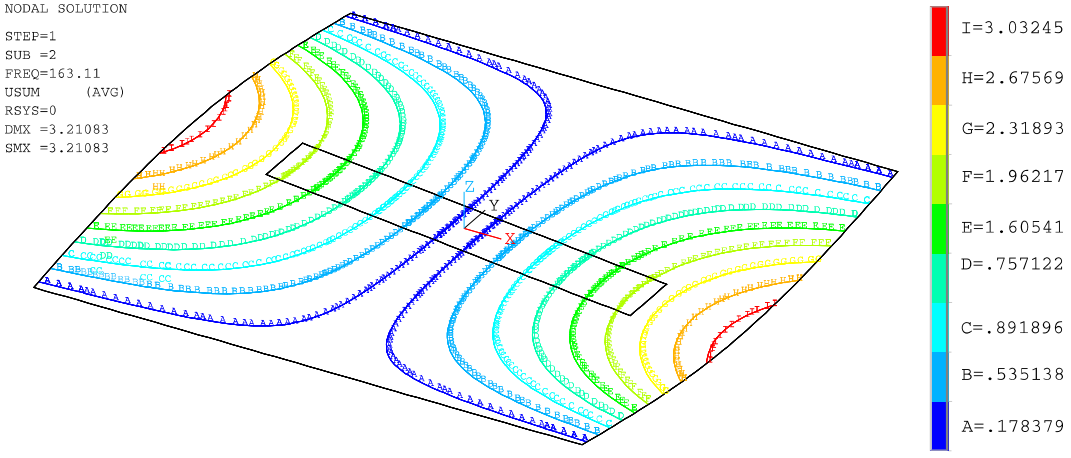

Fig. 30. Simulated modal response for the repaired panel: second mode, $\overline{f_2} = 163.1$ Hz.

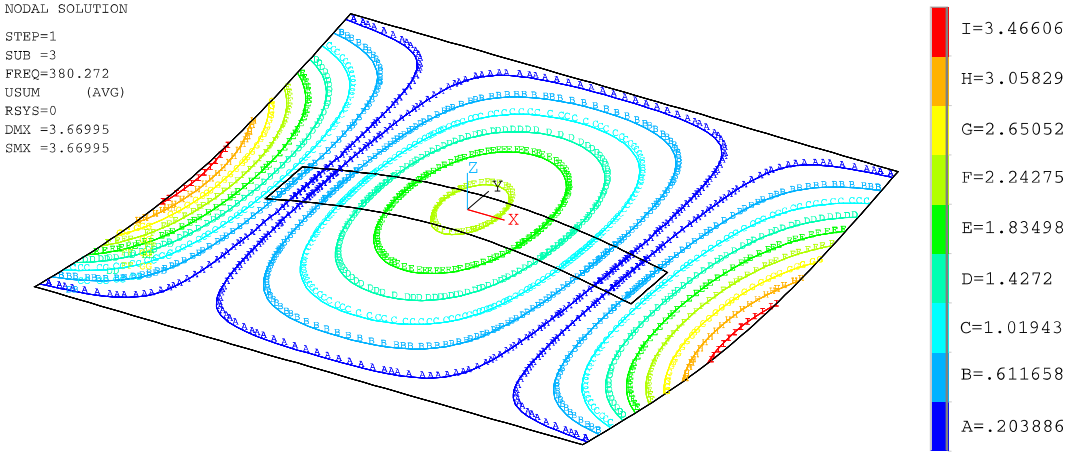

Fig. 31. Simulated modal response for the repaired panel: third mode, $\overline{f_3} = 380.3$ Hz.

References

[1] Alderliesten RC, Benedictus R. Fiber/metal composite technology for future primary aircraft structures. J Aircr 2008;45(4):1182–9. http://dx.doi.org/10.2514/1.33946.

[2] Jackson P, Munson K, Peacock L. Jane's All the world's Aircraft 2004–2005. London: Jane's Information Group; 2004.

[3] Jackson P, Bushell S, Willis D. IHS Jane's All the World's Aircraft 2014–2015: Development & Production. London: Jane's Information Group; 2014.

[4] Edwards T. Composite materials revolutionize aerospace engineering. Ingenia 2008;36:24–8, URL https://www.ingenia.org.uk/ingenia/issue-36/composite-materials-revolutionise-aerospace-engineering.

[5] Smith F. The use of composites in aerospace: Past, present, and future challenges. 2013, Avalon Consultancy Services ltd URL https://avaloncsl.files.wordpress.

com/2013/01/avalon-the-use-of-composites-in-aerospace-s.pdf.
[6] GAO. Aviation safety: Status of FAA's actions to oversee the safety of composite airplanes. Report GAO-11-849, US Government Accountability of Office; 2011.
[7] Barnes F, Walter DL. Reclaim and reuse strategies for carbon fibers. 2022, ASC - American Society of Composites webinar series on Sustainable Composite Design Competition - 2023.
[8] Gang L. Global carbon fiber composites market report. Market Report, Guangzhou, China: ATA CFT; 2023.
[9] Sauer M, Schüppel D. The global market for carbon fibers and carbon composites. Market Report, Dresden, Germany: Composites United; 2023.
[10] Katnam K, Da Silva L, Young T. Bonded repair of composite aircraft structures: A review of scientific challenges and opportunities. Prog Aerosp Sci 2013;61:26–42. http://dx.doi.org/10.1016/j.paerosci.2013.03.003.
[11] Baker AA. A summary of work on applications of advanced fibre composites at the aeronautical research laboratories, Australia. Composites 1978;9(1):11–6. http://dx.doi.org/10.1016/0010-4361(78)90512-8.
[12] Baker AA. Repair of cracked or defective metallic aircraft components with advanced fibre composites — an overview of Australian work. Compos Struct 1984;2(2):153–81. http://dx.doi.org/10.1016/0263-8223(84)90025-4.
[13] Baker AA, Callinan RJ, Davis MJ, Jones R, Williams JG. Repair of mirage III aircraft using the BFRP crack-patching technique. Theor Appl Fract Mech 1984;2(1):1–15. http://dx.doi.org/10.1016/0167-8442(84)90035-1.
[14] Baker AA. Fibre composite repair of cracked metallic aircraft components — practical and basic aspects. Composites 1987;18(4):293–308. http://dx.doi.org/10.1016/0010-4361(87)90293-X.
[15] Baker AA. Bonded composite repair of fatigue-cracked primary aircraft structure. Compos Struct 1999;47(1):431–43. http://dx.doi.org/10.1016/S0263-8223(00)00011-8.
[16] FAA. Acceptable methods, techniques, and practices - Aircraft inspection and repair. AC - Advisory Circular AC_43.13-1B. Washington, D.C.: U.S. Department of Transportation - Federal Aviation Administration; 1998, URL https://www.faa.gov/regulations_policies/advisory_circulars/index.cfm/go/document.information/documentid/99861.
[17] Ahn SH, Springer GS. Repair of composite laminates. Report, (DOT/FAA/AR-00/46). Washington, D.C.: U.S. Department of Transportation - Federal Aviation Administration; 2000, URL http://www.tc.faa.gov/its/worldpac/techrpt/ar00-46.pdf Approved for Public Release.
[18] Hasan ZF. Repair patch for composite structure and associated method. Patente US 2019/0232614 A1, Chicago: The Boeing Company; 2019, Pub. Jan. 17, 2019.
[19] Bertrand BA, Lewis AK. Structural pre-cured repair patch for repair to highly loaded primary and secondary structural components. (US 2019/0016107 A1). Chicago: The Boeing Company; 2019, Pub. Jan. 17, 2019.
[20] Ramji M, Srilakshmi R, Bhanu Prakash M. Towards optimization of patch shape on the performance of bonded composite repair using FEM. Compos Part B: Eng 2013;45(1):710–20. http://dx.doi.org/10.1016/j.compositesb.2012.07.049, URL https://www.sciencedirect.com/science/article/pii/S1359836812005033.
[21] da Silva DL, Echer L, Tanzi BNR, Marczak RJ, Iturrioz I. Experimental investigation of the structural performance of fiber-reinforced patches in the repair of locally damaged steel pipes. J Braz Soc Mech Sci Eng 2023;45(435):1–14. http://dx.doi.org/10.1007/s40430-023-04348-x, URL https://link.springer.com/article/10.1007/s40430-023-04348-x.
[22] Kumar AM, Hakeem S. Optimum design of symmetric composite patch repair to centre cracked metallic sheet. Compos Struct 2000;49(3):285–92. http://dx.doi.org/10.1016/S0263-8223(00)00005-2.
[23] Rachid M, Serier B, Bouiadjra BB, Belhouari M. Numerical analysis of the patch shape effects on the performances of bonded composite repair in aircraft structures. Compos Part B: Eng 2012;43(2):391–7. http://dx.doi.org/10.1016/j.compositesb.2011.08.047.
[24] Brighenti R, Carpinteri A, Vantadori S. A genetic algorithm applied to optimisation of patch repairs for cracked plates. Comput Methods Appl Mech Engrg 2006;196(1):466–75. http://dx.doi.org/10.1016/j.cma.2006.07.004.
[25] Bouchiba MSE, Serier B. A step towards the optimization of composite bonded repair shape using an estimation distribution approach. J Braz Soc Mech Sci Eng 2017;39:1755–71. http://dx.doi.org/10.1007/s40430-016-0599-2.
[26] Crothers PJ, Drechsler K, Feltin D, Herszberg I, Kruckenberg T. Tailored fibre placement to minimise stress concentrations. Compos Part A: Appl Sci Manuf 1997;28(7):619–25. http://dx.doi.org/10.1016/S1359-835X(97)00022-5, URL https://www.sciencedirect.com/science/article/pii/S1359835X97000225.
[27] Bittrich L, Seuffert J, Dietrich S, Uhlig K, Lisbôa Td, Kärger L, et al. On the resin transfer molding (RTM) infiltration of fiber-reinforced composites made by tailored fiber placement. Polymers 2022;14(22). http://dx.doi.org/10.3390/polym14224873, URL https://www.mdpi.com/2073-4360/14/22/4873.
[28] IPF-Dresden. Principle of tailored fiber placement. 2022, IPF: Leibniz-Institut für Polymerforschung Dresden, (Accessed 24 January 2024), https://tinyurl.com/IPF-Dresden-TFP.
[29] Xi J, Xia R, He Y, Yu Z. The fatigue repairing evaluation of hybrid woven composite patch with 2d&3D styles bonded al-alloy plates under UV and thermal curing. Compos Part B: Eng 2020;185:107743. http://dx.doi.org/10.1016/j.compositesb.2020.107743, URL https://www.sciencedirect.com/science/article/pii/S1359836819328756.
[30] Kim HJ, Kim HS, Lee GY, Kim MS, Min SH, Keller R, et al. Three-dimensional carbon fiber composite printer for CFRP repair. Compos Part B: Eng 2019;1–10. http://dx.doi.org/10.1088/1361-665X/ab2d08.
[31] Bekas DG, Sharif-Khodaei Z, Aliabadi FM. A smart multi-functional printed sensor for monitoring curing and damage of composite repair patch. Smart Mater Struct 2019;28(8):1–8. http://dx.doi.org/10.1016/j.compositesb.2019.106945.
[32] Li A, Lyu Y, Yang B, Yang D. Novel repair of bolted composite joints using 3D printed continuous fibre patches with custom fibre paths. Compos Part B: Eng 2025;295:112212. http://dx.doi.org/10.1016/j.compositesb.2025.112212, URL https://www.sciencedirect.com/science/article/pii/S1359836825001027.
[33] Katnam K, Comer A, Roy D, Da Silva L, Young T. Composite repair in wind turbine blades: an overview. J Adhes 2015;91(1–2):113–39. http://dx.doi.org/10.1080/00218464.2014.900449.
[34] Aabid A, Hrairi M, Ali JSM, Sebaey TA. A review on reductions in the stress-intensity factor of cracked plates using bonded composite patches. Materials 2022;15(9):3086. http://dx.doi.org/10.3390/ma15093086.
[35] CYCOM. Cycom® 5250-4 prepeg system. Technical Data Sheet, Alpharetta, Georgia: Cytec (Solvay Group); 2019.
[36] CYCOM. CYCOM® 977-3 Epoxy Resin System. Technical Data Sheet, Alpharetta, Georgia: Cytec (Solvay Group); 2018.
[37] HEXCEL. Hexcel® 3501-6 epoxy matrix. Product data sheet. Stamford, Connecticut: Hexcel Corporation; 2016.
[38] Gougeon Brothers I. West System® 105 Epoxy Resin / 209 Extra Slow Hardener. Technical Data Sheet, Bay City, Michigan: Gougeon Brothers Inc.; 2015.
[39] Daniel IM, Ishai O. Engineering mechanics of composite materials. Engineering mechanics of composite materials, vol. 13, Oxford: Oxford University Press; 2006, URL https://books.google.com.br/books?id=x5S_QgAACAAJ.
[40] Echer L, Souza CEd, Marczak RJ. A study on the best conventional shapes for composite repair patches. Mater Res 2021;24. http://dx.doi.org/10.1590/1980-5373-MR-2021-0304.
[41] Ahmad S, Irons BM, Zienkiewicz O. Analysis of thick and thin shell structures by curved finite elements. Internat J Numer Methods Engrg 1970;2(3):419–51. http://dx.doi.org/10.1002/nme.1620020310.
[42] Zienkiewicz OC, Taylor RL, Zhu JZ. The finite element method: its basis and fundamentals. Oxford: Elsevier; 2005, p. 752, URL https://books.google.com.br/books?id=YocoaH8lnx8C.
[43] Nocedal J, Wright SJ. Numerical optimization, second ed. Springer series in operations research and financial engineering, New York: Springer; 2006, p. 664. http://dx.doi.org/10.1007/978-0-387-40065-5.
[44] ASTM. D790-17 – Standard test methods for flexural properties of unreinforced and reinforced plastics and electrical insulating materials. Technical Report, West Conshohocken: ASTM International; 2017, p. 1–12. http://dx.doi.org/10.1520/D0790-17.